

Towards inline spatially resolved temperature sensing in thermal ablation with chirped fiber Bragg grating

Original

Towards inline spatially resolved temperature sensing in thermal ablation with chirped fiber Bragg grating / Tosi, Daniele; Korganbayev, Sanzhar; Zhakin, Nurlan; Gassino, Riccardo; Perrone, Guido; Vallan, Alberto. - ELETTRONICO. - (2016), pp. 1-6. (11th IEEE International Symposium on Medical Measurements and Applications, MeMeA 2016 University of Sannio, ita 2016) [10.1109/MeMeA.2016.7533777].

Availability:

This version is available at: 11583/2651959 since: 2016-10-06T11:48:01Z

Publisher:

Institute of Electrical and Electronics Engineers Inc.

Published

DOI:10.1109/MeMeA.2016.7533777

Terms of use:

This article is made available under terms and conditions as specified in the corresponding bibliographic description in the repository

Publisher copyright

(Article begins on next page)

Towards inline spatially resolved temperature sensing in thermal ablation with chirped fiber Bragg grating

Daniele Tosi, Sanzhar Korganbayev, Nurlan Zhakin
Nazarbayev University
School of Engineering
Astana, Kazakhstan
{daniele.tosi, skorganbayev, nzhakin}@nu.edu.kz

Riccardo Gassino, Guido Perrone, Alberto Vallan
Politecnico di Torino
Department of Electronics and Telecommunications
Torino, Italy
{riccardo.gassino, guido.perrone, alberto.vallan}@polito.it

Abstract—We investigate the theory and feasibility of an inline spatially resolved temperature sensor, suitable for thermal ablation monitoring. The sensor is based on a chirped fiber Bragg grating (CFBG). The CFBG is modelled as a chain of Bragg gratings, each sensitive to local temperature variations. By using a combination of iterative and statistical optimization techniques, it is possible to use demodulate the CFBG, in case of a Gaussian-like spatial temperature profile. A feasibility test based on CFBG simulation shows that the CFBG returns error <1 mm on cells damage threshold spatial estimation and good noise resilience.

Keywords—optical fiber sensors; fiber Bragg grating (FBG); chirped FBG (CFBG); distributed sensing; thermal ablation; interventional cancer care.

I. INTRODUCTION

Thermal ablation (TA) is an emerging procedure for cancer care. TA makes use of a radiofrequency [1-2], microwave [3], laser [4], or high-intensity focused ultrasound [5] source, and a miniaturized applicator, percutaneously inserted into the tissue. When the electrical or optical source is switched on, heat is produced at the tip(s) of the applicator, and transferred in the surrounding area by thermal induction and conduction [6]. In the recent years, TA has significantly increased its range of application in the treatment of hepatic [1, 7], pancreatic [4], lung, deep-seated brain [8] and other tumors.

Temperature is the key driver of TA. The mortality rate of cancer cells is directly dependent upon thermal dosimetry [9], a parameter that takes into account the temperature values and their persistence. For cancer care, 42-44°C is the threshold for cells damage, while 52°C for one minute is the typical clinical value for successful ablation of cells [10]. At 60°C cells death is nearly instantaneous, and this is the target temperature of TA procedures.

Despite the advantageous clinical properties of TA over resection, most recent studies agree that TA provides similar or better short-term performance than resection, but long-term effects (such as 5-year survival rate) do not achieve the same quality of invasive techniques; as an example, the study of Guglielmi *et al.* [11] that compares RF ablation and resection for liver tumors, shows that TA's 5-year survival rate is often half or lower than resection. One of the main reasons for this performance gap is the lack of monitoring during TA. In clinical procedures, temperature is either monitored with a

single thermocouple [12], or not monitored at all. Only with the last generation of RF-TA devices [13] multiple thermocouples are embedded on the ablation device tips, while thermal imaging with infrared camera [14] is viable only in *ex-vivo* studies.

It is therefore essential to improve thermal monitoring in TA, providing a real time sensing device that has 4 requirements: (1) miniature active size, to detect local temperatures rather than spatial averages; (2) miniature footprint and cabling, to avoid altering ablation shape; (3) biocompatibility, compliance with ISO 10993 standard, and MRI compatibility; (4) dense spatial resolution, to sample the temperature profile with the narrowest step.

Optical fiber sensors [15] are an excellent technology for this task, as optical fibers have microscopic size (40-250 μm diameter), and modern fibers have adequate tensile strength and bending insensitivity. Glass fibers are also chemically and biologically inert. While the first application of an optical fiber sensor in hyperthermia dates back to 2000 [16], most advances in the application of optical fiber sensing technology in TA have been reported in the last triennium [17-23].

Fiber Bragg gratings (FBGs) [16-17, 24] are the main and most popular in-line fiber-optic sensing technology. Thanks to wavelength division multiplexing (WDM) it is possible to operate several FBG sensors along an individual fiber. Thanks to the draw-tower fabrication method for FBGs [25] that has been recently industrialized by FBGS International. [26], it is possible to fabricate grating arrays having 1 cm spacing [17]. Despite the straightforward operation and detection of FBGs, the spatial resolution is relatively poor, for TA, whereas only 2-4 sensing points per fiber can be obtained; therefore, FBGs yield only a marginal improvements over thermocouples.

On the opposite side, distributed temperature sensing (DTS) techniques have been demonstrated; most notably, the white light interferometric setup for distributed demodulation of Rayleigh backscattering signature can achieve sub-millimeter spatial resolution over several meters of fiber length [27-28]. This DTS approach has been consolidated in the Luna OBR4600 instrument [29]. To date, the only application of a DTS in hyperthermia has been documented by Macchi *et al.* [19] in 2014. Compared to FBGs, the DTS has excellent spatial resolution (200 μm in [19]), but the cost of the interrogator is

higher than the TA setup itself; in addition, the DTS has a tight trade-off between accuracy, spatial resolution, and detection speed, which is restrictive for real-time measurements.

In this paper, the authors propose to use a chirped FBG (CFBG) [20, 24, 30], as temperature sensor for thermal ablation. The CFBG behaves as a dense cascade of grating structures inside an optical fiber. As opposite to a chain of FBGs, in which each grating reflects one wavelength, the CFBG returns a broadband spectrum that depends on all temperature values, in each point along the grating. This feature makes the CFBG attractive for sensing, because it can abate resolution limits of FBGs by two orders of magnitude; on the other hand, the demodulation of a CFBG, i.e. the discrimination of all temperature values in each point of the CFBG, is an unsolved problem. A first example of broadband CFBG used in RF ablation has been documented by Tosi *et al.* [20], with a simple decoding algorithm that, however, is effective only for a monotonic temperature pattern.

In this paper, we investigate a novel decoding scheme, based on a combination of iterative and statistical optimization. The algorithm works by applying an arbitrary temperature pattern and estimating its corresponding CFBG spectrum, refining the optimization through a series of steps until the estimated spectrum matches the measured spectrum. Preliminary results, performed on CFBG simulation [24], show that our demodulation approach can estimate the typical patterns generated during TA, typically having shape similar to a Gaussian or super-Gaussian function. A preliminary experimental measurement is also included.

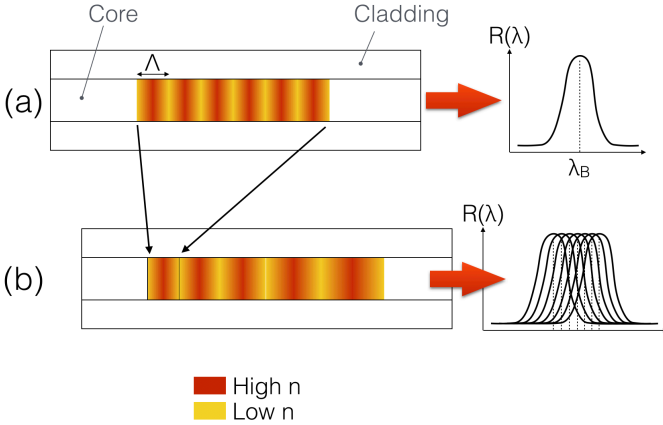


Fig. 1. Principle of operation of an FBG and CFBG. (a) FBG principle: a periodic modulation of the refractive index n , with period Λ , is generated inside the core of an optical fiber; the grating structure results in a single wavelength (λ_B) being reflected, while the remaining wavelengths are transmitted through the grating. The reflection spectrum $R(\lambda)$ is narrowly centered around λ_B . (b) CFBG principle: the CFBG behaves as a cascade of FBGs, each having different Λ . The resulting spectrum is the combination of all reflection spectra of each section of the grating, and therefore results in a broadband spectrum.

II. CFBG DISTRIBUTED SENSING

A. FBG and CFBG theory

An FBG is a periodic modulation of the refractive index of an optical fiber [15]. This periodic pattern with microscopic step induces a wavelength-selective behavior, which reflects

one wavelength and transmits the other wavelengths (Fig. 1a). To some extent, the FBG is the fiber-optic equivalent of notch electrical filters and band-stop microwave filters. Erdogan's coupled mode theory [24] provides an explicit expression for an FBG spectrum. For a grating having period Λ and effective refractive index n_{eff} , the Bragg wavelength $\lambda_{B,0}$, which corresponds to the peak of reflectivity is given by:

$$\lambda_{B,0} = 2n_{\text{eff}} \Lambda. \quad (1)$$

When a temperature or strain variation is applied, the Bragg wavelength shifts according to a linear relationship. Assuming that no strain stimuli are applied, and $\lambda_{B,0}$ is the Bragg wavelength in reference condition (i.e. ambient temperature), the resulting Bragg wavelength shifts as a function of temperature variation ΔT :

$$\lambda_B(\Delta T) = \lambda_{B,0} + \xi \cdot \Delta T \quad (2)$$

where the thermal sensitivity coefficient ξ has typical value of 10 pm/°C. Eq. (2) is the principle of operation of standard FBG sensors [15-17]. From the Bragg wavelength, [24] provides a closed-form expression for the reflection spectrum of an FBG

$$R(\lambda) = \frac{\sinh^2\left(L\sqrt{\kappa^2 - \sigma^2}\right)}{\cosh^2\left(L\sqrt{\kappa^2 - \sigma^2}\right) - \frac{\sigma^2}{\kappa^2}} \quad (3)$$

where: λ is the wavelength; $R(\lambda)$ is the reflectivity; L is the grating length; κL is the grating strength, a unitless number than typically ranges from 0.1 for weak grating to 4 for strong grating. If δn_{eff} is the amplitude of the refractive index modulation, σ has the following expression:

$$\sigma = \frac{\pi}{\lambda} \delta n_{\text{eff}} + 2\pi n_{\text{eff}} \left(\frac{1}{\lambda} - \frac{1}{\lambda_B} \right). \quad (4)$$

Eq. (1-4) provide a model for operation of a uniform FBG sensor. A chirped FBG, however, operates as in Fig. 1b: a chain of weak gratings, each having a slightly different wavelength, aligned as a cascade of filters. It is possible to approximate the CFBG as a cascade of Z FBG, aligned on the each having a different wavelength and each subjected to a different temperature variation. Hence, Eq. (2-4) are rewritten as:

$$\lambda_{B,z} = \lambda_{B,0,z} + \xi \cdot \Delta T_z \quad (5)$$

$$R_z(\lambda) = \frac{\sinh^2\left(L_z \sqrt{\kappa_z^2 - \sigma_z^2}\right)}{\cosh^2\left(L_z \sqrt{\kappa_z^2 - \sigma_z^2}\right) - \frac{\sigma_z^2}{\kappa_z^2}} \quad (6)$$

$$\sigma_z = \frac{\pi}{\lambda} \delta n_{\text{eff}} + 2\pi n_{\text{eff}} \left(\frac{1}{\lambda} - \frac{1}{\lambda_{B,z}} \right) \quad (7)$$

where the subscript $z = 1, 2, \dots, Z$ refers to each FBG composing the cascade. In this approach, the z -th FBG is subjected to its temperature variation ΔT_z , thus the CFBG has, inherently, the capability of discriminating the temperature pattern $\Delta T_1, \dots, \Delta T_Z$. In this work, we focus on CFBG with linear chirp, hence

$$\lambda_{B,0,z} = \lambda_{B,0,1} + \zeta z. \quad (8)$$

where ζ is the chirp coefficient. Typically, the linear pattern in Eq. 8 is achieved by varying the period of the refractive index modulation, with a linear profile.

From each spectrum of the cascade, it is finally possible to derive the overall spectrum of the CFBG, which is therefore dependent upon the whole set of temperature values $\Delta T_1, \dots, \Delta T_Z$:

$$R_{CFBG}(\lambda) = 1 - \prod_{z=1}^Z [1 - R_z(\lambda)]. \quad (9)$$

B. CFBG simulation

Assuming a grating having step-length $L_z = 0.1$ mm, and chirp coefficient $\zeta = 1.6$ nm/mm, increasing the length of the grating L results in an enlargement of the rejected bandwidth. For a weak grating ($\kappa_z L_z = 0.1$), Fig. 2 shows the CFBG spectrum for different length of the CFBG: starting from the leftmost wavelength (1540 nm), the grating is simulated by adding up a cascade of sections with length Z .

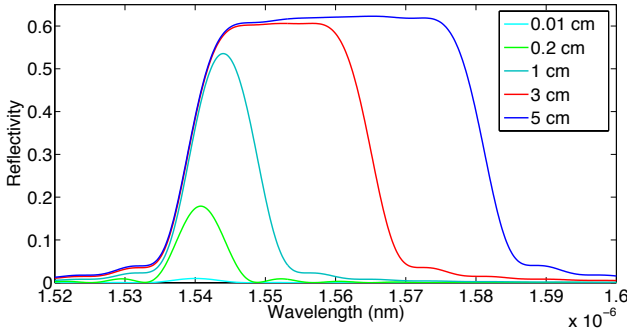


Fig. 2. Spectrum of the simulated CFBG structure, for different length of the grating L .

It is possible to show that, for a short number of grating sections, the CFBG simulation returns a spectrum similar to an apodized FBG [24], while increasing the number of sections over 100, as proposed in this paper, the CFBG returns a broadband spectrum. The bandwidth of the CFBG for 500 sections ($L = 5$ cm) is 40 nm, and this is the value that best approximates the CFBG used in experiments.

Fig. 3 shows the effect of the grating strength: assuming the parameter $\kappa_z L_z$ constant over the whole grating length ($L = 5$ cm), thus $\kappa_1 L_1 = \kappa_2 L_2 = \dots = \kappa_Z L_Z = \kappa L$, as in [20], the CFBG spectrum maintains the original broadband shape, but changes baseline reflectivity value. A weak grating having $\kappa L = 0.025$ achieves 6% reflectivity; conversely a strong chirped grating having $\kappa L = 0.25$, such as gratings fabricated on highly photosensitive fibers, has reflectivity saturating at 99.8%.

When κL varies from 0.1 to 0.18, the grating peak reflectivity varies from 62% to 95%. This choice of grating structure is the best for distributed sensing, when we aim at obtaining a significant variation of the optical spectrum as a function of thermal stimuli, and having a favorable signal-to-noise ratio (SNR). Highly reflective grating, by having a saturated reflectivity, yield minimum sensitivity to spatial temperature variations, as their reflectivity is saturated. Conversely, a weak CFBG has good thermal sensitivity but yields a low SNR.

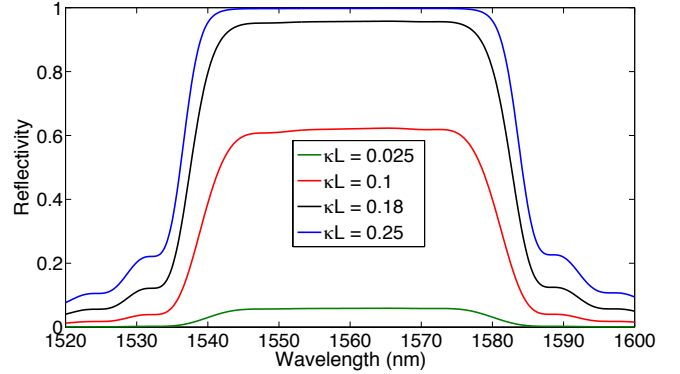


Fig. 3. CFBG spectrum, in absence of temperature variations, for different values of grating strength κL .

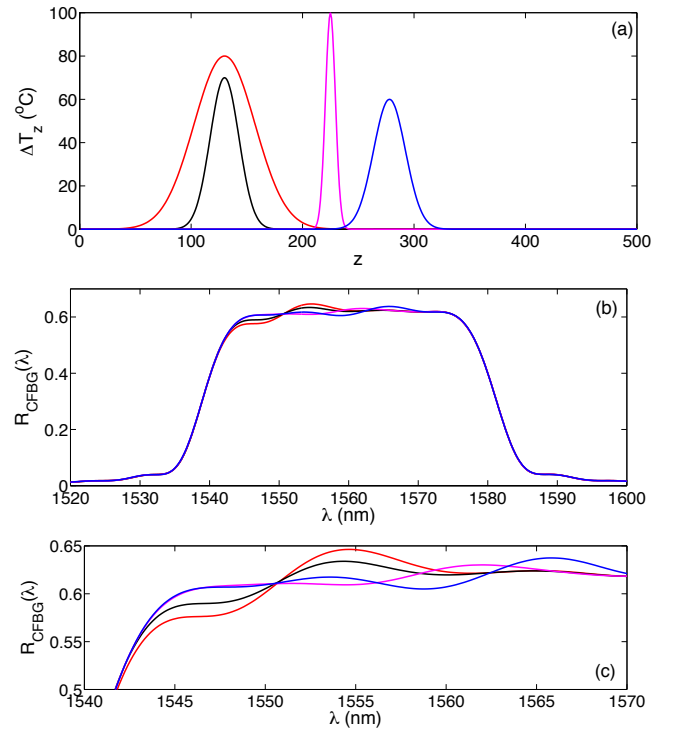


Fig. 4. Thermal-spatial sensitivity of the CFBG. (a) Different temperature profiles $\Delta T(z)$, having Gaussian shape and different variance, width, and amplitude, are applied on a the CFBG spectrum. (b) For each temperature profile, the corresponding reflective spectrum of the CFBG is computed. (c) Zoom on the inner region.

C. Thermal sensitivity

Unlike uniform gratings, the CFBG spectrum significantly changes as a function of both temperature, and its spatial distribution. Fig. 4 shows the thermal-spatial sensitivity,

computed for a 5-cm long CFBG having $\kappa L = 0.1$. In Fig. 4(a) several patterns are applied, having Gaussian shape with different amplitudes and width, and having peak position shifting along z . Fig. 4(b-c) show the corresponding variations on the reflection spectrum. When a temperature pattern is applied, the spectrum exhibits a deformation similar to a first-order Bessel function. The peak position of the spectral deformation depends on the temperature peak along z axis, while the amplitude and width of such deformation are jointly encoded in the spectrum. Fig. 4 shows the principle of operation of the CFBG applied to distributed sensing, as the CFBG spectrum depends on the whole ΔT_z envelope.

III. CFBG DEMODULATION

Instead of using a complete CFBG demodulation, using algorithms such as reversed layer peeling [33], which would lead to an unbearable computational effort, we rely on the physical principles of mini-invasive TA procedures: in hyperthermia, as well as in other medical measurements, the temperature profile ΔT_z is strictly tied to the physical phenomena occurring during the measurement. In TA, when the CFBG sensor is positioned longitudinally along the TA applicator [17, 20, 22-23], or perpendicularly [19] the temperature pattern typically has a peak in proximity of the ablation tip, and then decreases on both sides. In a first guess, we can approximate the spatial temperature pattern with a Gaussian function of this form:

$$\Delta T_{guess}(z) = B \exp \left[-\frac{(z-A)^2}{C} \right]. \quad (10)$$

By using a guess function, we switch from the task of identifying the whole Z -size set of ΔT_z values, to identifying only 3 parameters (A , B , C). A guess function of such form can, to a certain degree, approximate the spatial temperature pattern occurring during percutaneous laser ablation [22] and RF ablation of hard tissues [2].

The underlying principle of CFBG sensing is to turn the demodulation task into an optimization problem, such as the minimization of a cost function (CF). To accomplish this task, we consider the CFBG spectrum measured by the spectrometer $R_{MEAS}(\lambda)$, and the spectrum calculated by selecting an arbitrary pattern ΔT_z into Eq. (5) and calculating the CFBG spectrum $R_{CALC}(\lambda)$ by means of Eq. (6). We select as CF the following function

$$CF = \sum_{\lambda} \left[R_{CALC}(\lambda) - R_{MEAS}(\lambda) \right]^2 \quad (11)$$

in which the squared difference between the spectra is sampled in each point of the wavelength grid. The goal is then to generate the temperature spatial distribution ΔT_z that minimizes CF.

In the first step, we keep the temperature pattern tied to Eq. (10) guess function, and we progressively estimate the 3 parameters A , B , and C (in this order). This task is accomplished by fixing two parameters to an arbitrary value, and changing the third parameter until CF is minimized. At the

end of this step, we obtain the parameter set (A_1 , B_1 , C_1) that “individually” minimize CF.

In order to refine the estimate and further reduce CF, a Monte Carlo approach is used: a number N of (A , B , C) sets are randomly generated, distributed within ($A_{opt} \pm 5\%$, $B_{opt} \pm 5\%$, $C_{opt} \pm 10\%$). Simulations show that around 4% of values hereby generated improve the CF obtained in the purely iterative step, and this value largely depend on the tolerances set on A , B , C . At this stage, the estimate on ΔT_z is refined.

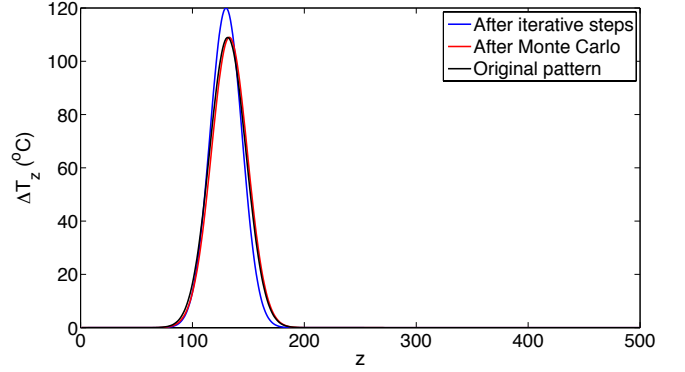


Fig. 5. Effectiveness of the reconstruction algorithm on a Gaussian-shaped temperature profile. The chart shows the original pattern, as well as the temperature distribution estimated after the first iterative stage, and after the second Monte Carlo stage.

Fig. 5 shows the effectiveness of the CFBG demodulation, on an arbitrary temperature pattern having Gaussian shape. The iterative steps return a Gaussian function that approximates the original pattern; and 150-size Monte Carlo contributes in improving the estimate, reducing the detection error below 1%. Most importantly, for TA procedures, is the estimation of the width of the temperature pattern, particularly in correspondence of 23°C and 40°C: these are the approximate values for damage threshold of TA procedures *in vivo* and *ex vivo*, where temperature variation exceeds the body temperature and ambient temperature, respectively. We consider as threshold $\Delta T_z = 40^\circ\text{C}$, and compute the difference in crossing the threshold on left and right sides between the original ΔT_z function and the estimated ΔT_z functions with iterative methods and iterative + Monte Carlo approach. In the first case, the error is 0.02 mm on the left side and 0.34 mm on the right side; when Monte Carlo is applied, the error changes to 0.12 mm on the left side, and 0.11 mm on the right side. In all instances of Gaussian-like patterns, the threshold error is well confined below 1 mm, and is typically <0.2 mm after applying Monte Carlo.

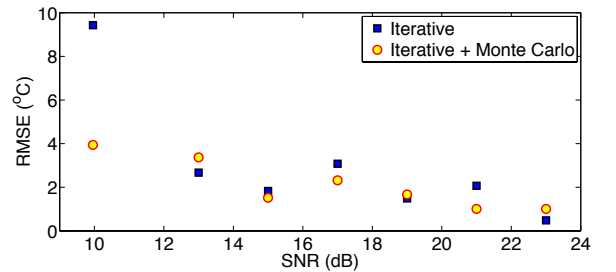


Fig. 6. Root mean square error (RMSE) between applied and reconstructed temperature patterns, as a function of SNR.

In practical applications, measured spectra are corrupted by noise; we define the SNR as the ratio between the peak reflectivity and noise variance. Fig. 6 shows the effect of noise on CFBG decoding: the root mean square error (RMSE) between measured and reconstructed spectra is plotted as a function of SNR. It is possible to show that the use of Monte Carlo is effective in reducing the RMSE, and for SNR as low as 10 dB the iterative algorithm exhibits performance decay.

It is possible to improve the CFBG demodulation by acting on both the guess function in Eq. (10), and on CF in Eq. (11). Replacing the guess function with a super-Gaussian pattern

$$\Delta T_{guess}(z) = E \exp \left| -\frac{(z-D)^{2G}}{F} \right| \quad (12)$$

and applying the sequential + Monte Carlo decoding to the 4 parameter set (D, E, F, G) can better approximate RF ablation of soft tissues [6, 19].

IV. PRELIMINARY EXPERIMENTS

In this section, a preliminary experimental characterization is shown. The setup in Fig. 7 is used to interrogate the CFBG: a superluminescent light-emitting diode (SLED) is used as light source (Exalos EXS2100, with control board Exalos EBD-series). Light is coupled through a 3-dB 1x2 optical coupler, and transmitted to the CFBG. The backreflection is collected with a FBG analyzer (Bayspec FBGA-IRS) [31] and data acquisition (DAQ) is performed via LabVIEW. The CFBG used in experiments is provided by Technica S. A., and has 5 cm length with 95% maximum reflectivity and ~8 nm/cm chirp rate.

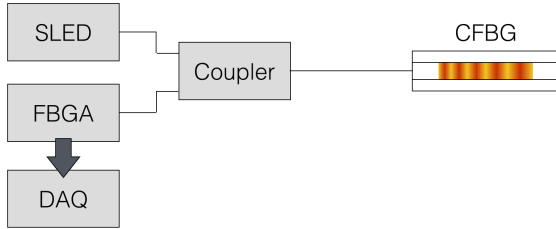


Fig. 7. Optical setup used for CFBG interrogation.

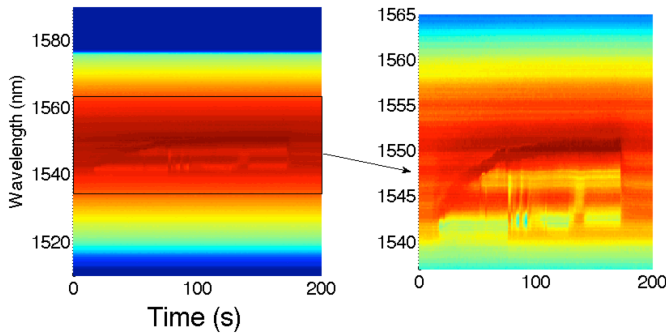


Fig. 8. Experiment using CFBG in laser ablation (LA). The left chart reports the whole CFBG spectrum, during a LA experiment; the spectrum is reported on the vertical axis, as a color plot (blue = low reflectivity, red = high reflectivity), while on the horizontal axis the elapsed time is shown. The right chart shows an inset on the reflection peak in the CFBG spectrum.

Fig. 8-9 investigate the feasibility of CFBG as sensor for laser ablation (LA). A setup with a 1064-nm laser, with standard single-mode delivery fiber, has been prepared to perform ablation on porcine pancreas tissue. The CFBG has been inserted in parallel with the LA delivery fiber, having the CFBG center positioned in proximity of the ablation peak. Fig. 8 shows the evolution of the CFBG spectrum during LA, for a duration of 200s. It is possible to show, in the inset of Fig. 8, that the wavelength shift in the inner part of the CFBG spectrum has an almost exponential growth, as in [4] for a solid-state laser and in [21] for a diode-pumped fiber laser. Such results are highlighted in Fig. 9, where the inner part of the CFBG spectrum changes shape as the LA procedure evolves.

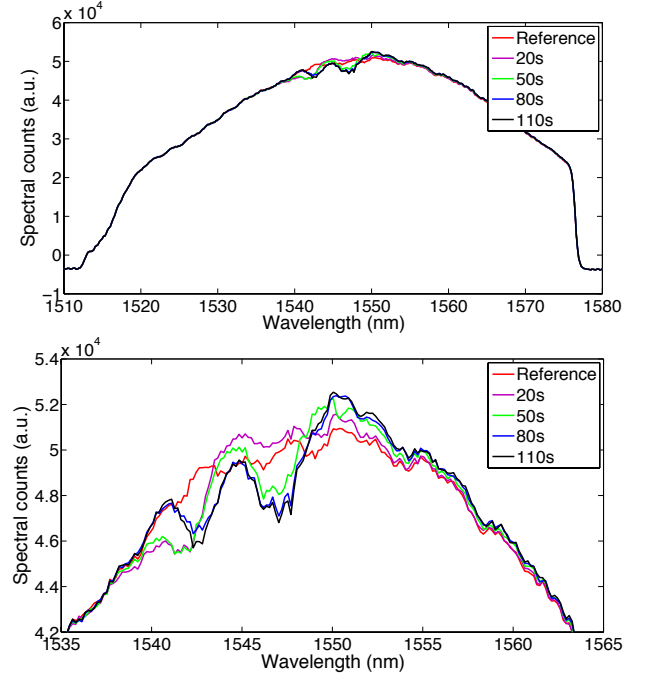


Fig. 9. CFBG spectrum during laser ablation. The upper chart shows the optical spectrum, as recorded by FBG analyzer, sampled over 1510-1580 nm wavelength grid, for different values of ablation time. The lower chart shows the high-reflectivity inner portion of the spectrum.

V. CONCLUSIONS

A modern and effective approach to mini-invasive thermal ablation in cancer care requires a real-time, in-vivo capillary temperature monitoring at the point of treatment, in order to measure in real time the surface or volume of tissue exposed to ablation, and predict the TA outcome. We propose a fiber-optic CFBG sensor for such task; this device owns the advantageous properties of fiber-optic sensors, and shows the premises to high-density thermal sensing. Our simulations, carried out by modeling the CFBG as a cascade of FBG, show the premises for distributed sensing, as the CFBG has a reflection spectrum that depends on each local temperature value. We have set up a simple but effective software for CFBG demodulation, based on a semi-iterative approach complemented by Monte Carlo optimization. This method can effectively decode the CFBG in presence of quasi-Gaussian or super-Gaussian temperature patterns, as typically achieved in mini-invasive TA. The results show the premises of an all-fiber sensor that can

instantaneously detect temperature with sub-mm resolution, and estimate the radius of TA-treated tissue with <0.2 mm error.

REFERENCES

- [1] P. L. Pereira, "Actual role of radiofrequency ablation of liver metastases," *Eur. Radiol.*, vol. 7, pp. 291-299, 2007.
- [2] B. J. Wood, J. R. Ramkaransingh, M. S. Tito Fojo, M. M. Walther and S. K. Libutti, "Percutaneous tumor ablation with radiofrequency," *Cancer*, vol. 94, pp. 443-451, 2002.
- [3] R. C. G. Martin, C. R. Scoggins, and K. M. McMasters, "Safety and efficacy of microwave ablation of hepatic tumors: a prospective review of a 5-year experience," *Ann. Surg. Oncol.*, vol. 17, no. 1, pp. 171-178, 2009.
- [4] P. Saccomandi, E. Schena, M. A. Caponero, F. M. Di Matteo, M. Pandolfi, M. Martino, and S. Silvestri, "Theoretical analysis and experimental evaluation of laser-induced interstitial thermotherapy in ex vivo porcine pancreas," *IEEE Trans. Biomed. Eng.*, vol. 59, no. 10, pp. 2958-2964, 2012.
- [5] Y. F. Zhou, "High intensity focused ultrasound in clinical tumor ablation," *World J. Clin. Oncol.*, vol. 10, 2011.
- [6] E. G. Macchi, M. Gallati, G. Braschi, A. Cigada, L. Comolli, "Temperature distribution during RF ablation on ex vivo liver tissue: IR measurements and simulations," *Heat Mass Transf.*, vol. 51, pp. 611-620, 2015.
- [7] S. N. Goldberg, G.S. Gazelle, C.C. Compton, P.R. Mueller, and K.R. Tanabe, "Treatment of intrahepatic malignancy with radiofrequency ablation," *Cancer*, vol. 88, no. 11, pp. 2452-2463, 2000.
- [8] Y. Anzai, R. Lufkin, A. DeSalles, D. R. Hamilton, K. Farahani, and K. L. Black, "Preliminary experience with MR-guided thermal ablation of brain tumors," *Am. J. Neurorad.*, vol. 16, pp. 39-48, 1995.
- [9] M. W. Dewhirst, B. L. Viglianti, M. Lora-Michiels, M. Hanson, M., and P. J. Hoopes, "Basic principles of thermal dosimetry and thermal thresholds for tissue damage from hyperthermia," *Int. J. Hyperthermia*, vol. 19, pp.267-294, 2003.
- [10] S. A. Sapareto, "Thermal dose determination in cancer therapy," *Int. J. Radiat. Oncol. Bio. Phys.*, vol. 10, pp. 787-800, 1984.
- [11] A. Guglielmi, A. Ruzzenente, A. Valdegamberi, S. Pachera, T. Campagnaro, M. D'Onofrio, E. Martone, P. Nicoli, and C. Iacono, "Radiofrequency ablation versus surgical resection for the treatment of hepatocellular carcinoma in cirrhosis," *J. Gastrointest. Surg.*, vol. 12, pp. 192-198, 2008.
- [12] M. J. Dodd, "Radiofrequency ablation of the liver: current status," *Am. J. Roentgen.*, vol. 176, pp. 3-16, 2001.
- [13] Starburst RFA MRI, <http://www.angiodynamics.com/products/starburst-mri>.
- [14] K. Ogan, W. R. Roberts, D. M. Wilhelm, L. Bonnell, D. Leiner, G. Lindberg, L. R. Kavoussi, and J. A. Cadeddu, "Infrared thermography and thermocouple mapping of radiofrequency renal ablation to assess treatment adequacy and ablation margins," *Urology*, vol. 62, pp. 146-151, 2003.
- [15] E. Udd and W. B. Spillman, *Fiber Optic Sensors: An Introduction for Engineers and Scientists*, 2nd edition, Wiley Interscience, 2011.
- [16] D. J. Webb, S. Jones, L. Zhang, I. Bennion, M. W. Hathaway, and D. A. Jackson, "First in-vivo trials of a fiber Bragg grating based temperature profiling system," *J. Biomed. Opt.*, vol. 5, no. 1, pp. 45-50, 2000.
- [17] D. Tosi, E. G. Macchi, M. Gallati, G. Braschi, A. Cigada, S. Poeggel, G. Leen, and E. Lewis, "Monitoring of radiofrequency thermal ablation in liver tissue through fibre Bragg grating sensors array," *Electron. Lett.*, vol. 50, no. 14, pp. 981-983, 2014.
- [18] D. Tosi, E. G. Macchi, and A. Cigada, "Fiber-optic temperature and pressure sensors applied to radiofrequency thermal ablation in liver phantom: methodology and experimental measurements," *J. Sens.*, vol. 2015, 909012, 2015.
- [19] E. G. Macchi, D. Tosi, G. Braschi, M. Gallati, A. Cigada, G. Busca, and E. Lewis, "Optical fiber sensors-based temperature distribution measurement in ex vivo radiofrequency ablation with submillimeter resolution," *J. Biomed. Opt.*, vol. 19, no. 11, 117004, 2014.
- [20] D. Tosi, E. G. Macchi, M. Gallati, G. Braschi, A. Cigada, S. Rossi, G. Leen, and E. Lewis, "Fiber-optic chirped FBG for distributed thermal monitoring of ex-vivo radiofrequency ablation of liver," *Biomed. Opt. Expr.*, vol. 5, no. 6, pp. 1799-1811, 2014.
- [21] Y. Liu, H. Yu, R. Gassino, A. Braglia, M. Olivero, D. Tosi, A. Vallan, and G. Perrone, "Characterization of tumour laser ablation probes with temperature measuring capabilities," *3rd International Conference on BioPhotonics*, 2015.
- [22] P. Saccomandi, E. Schena, and S. Silvestri, "Techniques for temperature monitoring during laser-induced thermotherapy: an overview," *Int. J. Hyperthermia*, vol. 29 no. 7, pp. 609-619, 2013.
- [23] D. W. Wang, P. G. Jia, Z. G. Ma, L. F. Xie, and Q. B. Liang, "Tip-sensitive fibre-optic Bragg grating ultrasonic hydrophone for measuring high-intensity focused ultrasound fields," *Electron. Lett.*, vol. 50, no. 9, pp. 649-650, 2014.
- [24] T. Erdogan, "Fiber grating spectra," *J. Lightw. Technol.*, vol. 15, no. 8, pp. 1277-1294, 1997.
- [25] E. Lindner, A. Hartung, D. Hoh, C. Chojetzki, K. Schuster, J. Bierlich, and M. Rothhardt, "Trends and future of fiber Bragg grating sensing technologies: tailored draw tower gratings (DTGs)," *Proc. SPIE*, vol. 9141, 2014.
- [26] FBGS International, <http://www.fbgs.com>.
- [27] M. E. Froggatt, D. K. Gifford, S. Kreger, M. Wolfe, and B. J. Soller, "Characterization of polarization-maintaining fiber using high-sensitivity optical-frequency-domain reflectometry," *J. Lightw. Technol.*, vol. 24, no. 11, pp. 4149-4154, 2006.
- [28] J. Soller, D. K. Gifford, M. S. Wolfe, and M. E. Froggatt, "High resolution optical frequency domain reflectometry for characterization of components and assemblies," *Opt. Expr.*, vol. 13, no. 2, pp. 666-674, 2005.
- [29] Luna Inc., OBR 4600, <http://lunainc.com/obr4600>.
- [30] Y. Okabe, R. Tsuji, and N. Takeda, "Application of chirped fiber Bragg grating sensors for identification of crack locations in composites," *Composit. Part A*, vol. 35, no. 1, pp. 59-65, 2004.
- [31] Bayspec FBGA, <http://www.bayspec.com/telecom-fiber-sensing/fbga-systems/>.
- [32] Ibsen I-MON, <http://ibsen.com/products/interrogation-monitors/i-mon-oem/i-mon-256-oem/>.
- [33] J. Skaar and K. M. Risvik, "A genetic algorithm for the inverse problem in synthesis of fiber gratings," *J. Lightwav. Technol.*, vol. 16, no. 10, pp. 1928-1932, 1998.